course, very large, but it is most unlikely that any combination of experimental errors could account for this discrepancy. It is unlikely that the reaction of hydrogen peroxide with S(IV), as observed in our field experiments, is catalysed by weak organic acids (the reaction taking place in cloud at GDF does not appear to be subject to general acid catalysis). Our conclusion is therefore that the oxidation by peroxide of SO_2 in cloud droplets to produce sulphuric acid is extremely rapid.

This work was supported by the Department of the Environment and the NERC.

Received 4 August; accepted 2 November 1988.

1. *SO_2, NO and NO_2 Oxidation Mechanisms: Atmospheric considerations* (ed. Calvert, J. G.) Acid Precipitation series Vol. 3 (Butterworth, Stoneham, Massachusetts, 1984).
2. Penkett, S. A., Jones, B. M. R., Brice, K. A. & Eggleton, A. E. J. *Atmos. Envir.* **13**, 123-137 (1979).
3. Middleton, P., Kiang, C. S. & Mohnen, V. A. *Atmos. Envir.* **14**, 463-472 (1980).
4. Chameides, W. L. & Davis, D. D. *J. geophys. Res.* **87**, 4863-4877 (1982).
5. Ames, D. L. *Central Electricity Generating Board Rep. no. TPRD/L/2552/N83* CERL Laboratories, Leatherhead, England (1983).
6. Lazrus, A. L., Kok, G. L., Gitlin, S. N., Lind, J. A. & McLaren, S. E. *Anal. Chem.* **57**, 917-922 (1985).
7. Kadlecek, J., McLaren, S., Camarota, N., Mohnen, V. & Wilson, J. *Proc. 4th Int. Conf. on Precipitation Scavenging* Santa Monica A Vol. 1 (1983).
8. Daum, P. H., Kelly, T. J., Schwartz, S. E. & Newman, L. *Atmos Envir.* **18**, 2671-2684 (1984).
9. Kelly, T. J., Daum, P. H. & Schwartz, S. E. *J. geophys. Res.* **90**, 7861-7871 (1985).
10. Choularton, T. W. *et al. Q. J. R. met. Soc.* **112**, 131-148 (1986).
11. Lazrus, A. L. *et al. Anal. Chem.* **58**, 594-597 (1985).
12. Heikes, B. G., Kok, G. L., Walega, J. G. & Lazrus, A. L. *J. geophys. Res.* **92**, 915-931 (1987).
13. Mader, P. M. *J. Am. chem. Soc.* **80**, 2634-2639 (1985).
14. Hoffman, M. R. & Edwards, J. O. *J. phys. Chem.* **79** 2096-2098 (1975).
15. Martin, L. R. & Damschen, D. E. *Atmos. Envir.* **15**, 1615-1621 (1981).
16. McArdle, J. V. & Hoffmann, M. R. *J. phys. Chem.* **87**, 5425-5429 (1983).
17. National Bureau of Standards *NBS tech. Note* 270-1 124 (1965).
18. Gervat, G. P. *et al. Nature* **333**, 241-243 (1988).
19. Hill, T. A., Choularton, T. W. & Penkett, S. A. *Atmos. Envir.* **20**, 1763-1771 (1986).

Chemically sensitive structure-imaging with a scanning transmission electron microscope

S. J. Pennycook & L. A. Boatner

Solid State Division, Oak Ridge National Laboratory, PO Box 2008, Oak Ridge, Tennessee 37831-6024, USA

Conventional high-resolution electron microscopy uses the phase-contrast method[1], in which the diffracted beams emerging from the sample are recombined on the viewing screen of the microscope. The resultant contrast depends on the relative phases of the diffracted beams, which is sensitive to microscope and sample parameters, so that images must be interpreted by means of simulation, and defect models are somewhat empirical. By using a high-angle detector in a scanning transmission electron microscope, these problems may be avoided and high atomic-number contrast may be obtained. Here we present results of this technique applied to single crystals of the high-transition-temperature superconductors $YBa_2Cu_3O_{7-x}$ and $ErBa_2Cu_3O_{7-x}$. The heavy-atom planes are directly imaged as bright lines, and the probable structure of an observed defect is directly inferred from its image.

In the phase-contrast method of high-resolution electron microscopy, introduced by Scherzer[1], the contrast is controlled by the sample thickness and objective lens defocus as well as the atomic positions and species, so that phase-contrast images must be interpreted through image simulation, and defect models are often suggested by intuitition or from known defects in structurally similar materials. The high-angle annular detector of a scanning transmission electron microscope (STEM) avoids these structure-sensitive effects by detecting the electrons scattered, predominantly elastically, through high angles. The (incoherent) scattering at such small impact parameters occurs from largely unscreened nuclei, and therefore gives an image showing strong atomic-number (Z) contrast with a minimum dependence on specimen thickness and microscope defocus. Such a detector

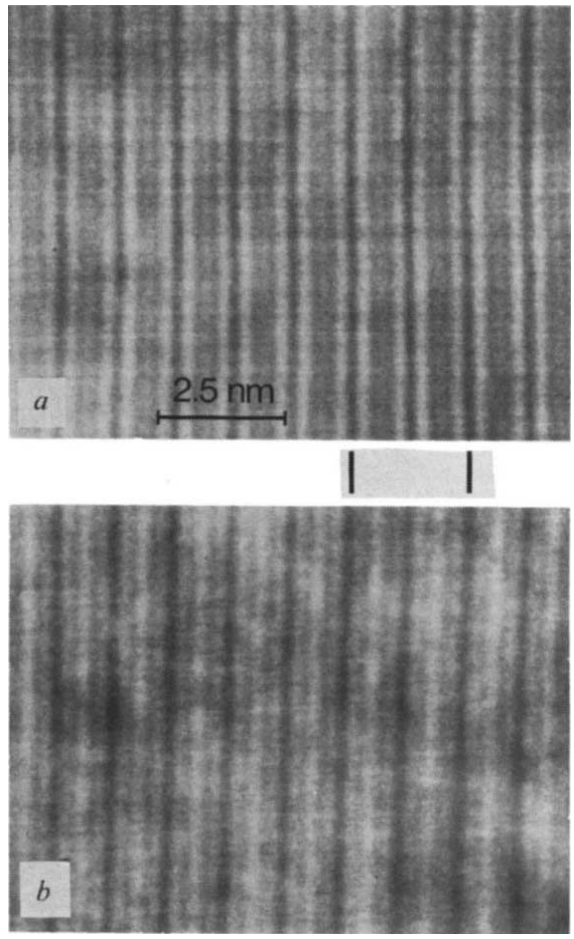

Fig. 1 Z-contrast STEM images of *a*, $YBa_2Cu_3O_{7-x}$ and *b*, $ErBa_2Cu_3O_{7-x}$ single crystals viewed parallel to the *c* planes (probe size ~0.25 nm, incident beam convergence semi-angle = 6 mrad, detector semi-angles = 50–150 mrad).

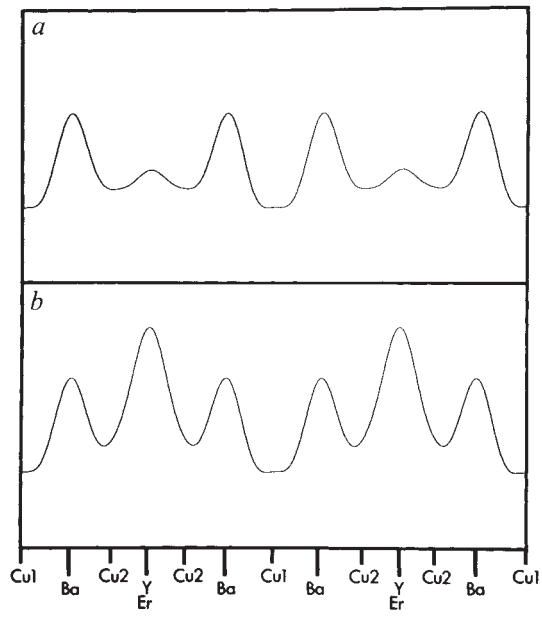

Fig. 2 Calculated image intensity across two unit cells of *a*, $YBa_2Cu_3O_{7-x}$ and *b*, $ErBa_2Cu_3O_{7-x}$, assuming no electron-channelling effects. Traces should be compared to the images in Fig. 1 between the vertical markers.

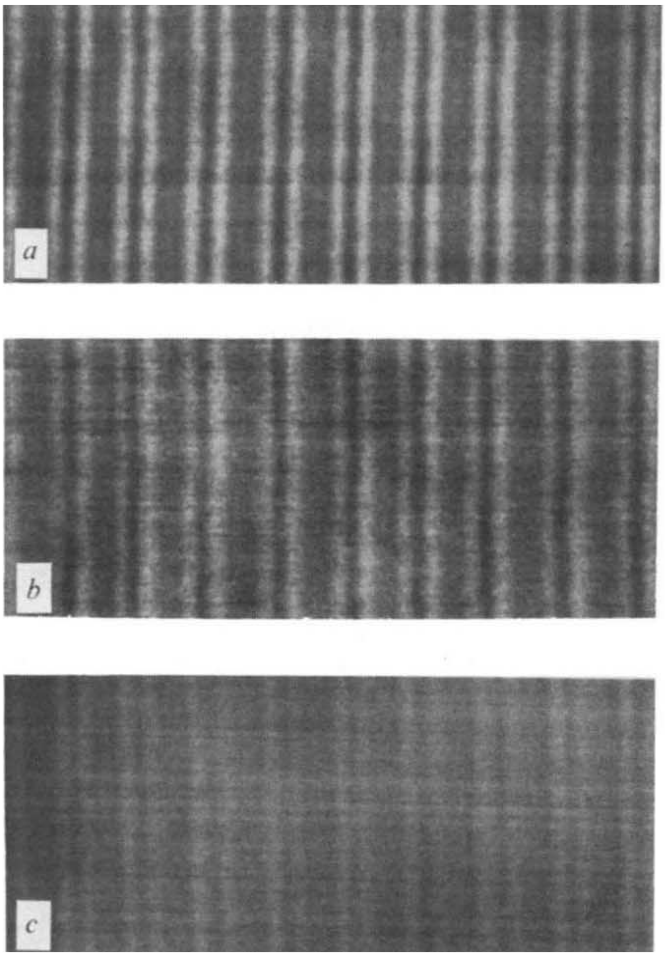

Fig. 3 *Z*-contrast STEM image of $YBa_2Cu_3O_{7-x}$ at thicknesses of *a*, 4 nm, *b*, 27 nm, *c*, 40 nm.

has been used to image, without resolving the crystal structure, supported-catalyst particles[2,3] and dopants in solution in silicon[4,5]. Using a new high-resolution pole piece (spherical-aberration coefficient $C_s \approx 1.3$ mm) and tilting holder in a VG Microscope's HB501 STEM, operating at 100 keV, we have been able to form a probe of <0.25-nm diameter (measured from images of single uranium atoms supported on a thin carbon film) and have obtained the first images that resolve a crystal lattice while preserving the strong *Z*-contrast characteristic of high-angle electron scattering.

Figure 1 shows images from cross-sections of $YBa_2Cu_3O_{7-x}$ and $ErBaCu_3O_{7-x}$ viewed parallel to the *c* (layer) planes; the materials were prepared by mechanical polishing followed by Ar-ion milling. The tripled perovskite cell is clearly visible, the bright lines within the cell corresponding to the planes containing the heavy metal ions. Because of the strong *Z*-sensitivity, the Y-atom ($Z = 39$) plane shows a lower intensity than the Ba ($Z = 56$) planes (Fig. 1*a*), whereas in the rare-earth-substituted material the Er ($Z = 68$) plane is brighter than the Ba planes (Fig. 1*b*). In the limit of a very thin crystal, the *Z*-contrast image would be given by the projected scattering power of the crystal convoluted with the probe intensity profile. Figure 2 shows calculated intensity profiles across two unit cells for the two superconductors, assuming a gaussian probe of 0.24-nm diameter at 1/e intensity and using a screened cross-section expression formulated by Fleischmann[5], which gives the best fit to experimentally measured cross-sections[6]. This extremely simple calculation reproduces correctly the relative intensities of the various planes seen in Fig. 1. It is analogous to the phase-grating approximation in phase-contrast imaging,

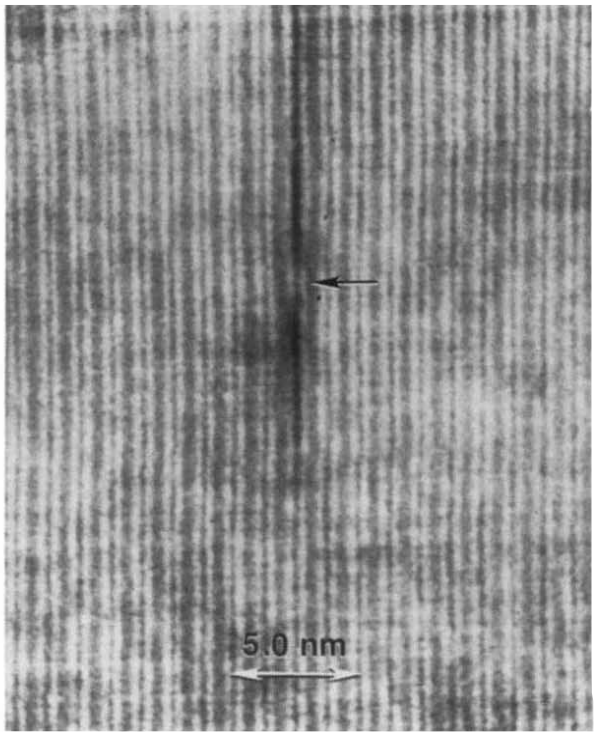

Fig. 4 *Z*-contrast STEM image of a planar defect in the $YBa_2Cu_3O_{7-x}$ single crystal. Above the arrow the Ba planes are expanded by $c/6$, but below the arrow they are not.

although it holds to significantly greater thicknesses, because for the first 5 nm or so the electron-channelling phenomenon simply concentrates the electron flux equally onto the various atomic planes in the unit cell. At greater thicknesses the flux oscillates between the various planes, concentrating first on the Ba planes at the expense of the Y plane, and then returning to the Y plane at thicknesses >30 nm. This introduces a thickness dependence in the image, although it is minimized because the image is formed from the integrated scattering throughout the whole sample thickness. Figure 3 shows images at 4, 27 and 40 nm, indicating that the absolute contrast reduces with increasing thickness because of electron absorption, whereas the relative contrast of the Y plane compared to the Ba planes is first reduced and then returns to its original level. This dependence is much less pronounced than in conventional phase-contrast imaging, and the various planes in the cell can be located even in samples 80 nm thick. The dependence of the image on objective-lens defocus is also significantly less than in a conventional phase-contrast image. It serves only to focus the probe on the sample and cannot produce contrast reversals.

In addition to strong chemical sensitivity, the highly localized nature of the electron scattering used in *Z*-contrast imaging is an advantage when studying defects or interfaces. In a conventional phase-contrast image, the localization is determined by the objective-lens defocus, which also controls contrast and resolution. Figure 4 shows a planar defect in the $YBa_2Cu_3O_{7-x}$ single-crystal cross-section. At this crystal thickness the Y plane is not visible, although the defect is unambigously seen to lie between the twin Ba planes of the unit cell. The defect expands the Ba planes by $c/6$ (where c is the undistorted lattice parameter) indicating that it is an interstitial-type defect. The dark contrast indicates that the defect must consist of atoms lighter than Y, and the structure immediately suggested is one in which an additional CuO layer is inserted between the Ba planes. This structure has also been proposed from conventional phase-contrast electron microscopy, and is suggested to arise as the response of the material to oxygen sub-stoichiometry[7] and as a

degradation reaction[8]. Interstitial cation layers and cationic disorders have also been reported[9,10], although we see no evidence of these. The $c/6$ expansion is only present in the upper part of Fig. 4 (above the arrow); the lower region of the defect does not dilate the lattice, although dark contrast remains. This lower region cannot correspond to simply an interstitial CuO layer, and we believe that the effect here is due to a degradation reaction, whereas the interstitial CuO plane seen in the upper part of the defect represents the fundamental response of the material to oxygen sub-stoichiometry, as proposed in ref. 7. This interpretation is supported by the recent observation of an ordered array of such defects[11].

We are grateful to M. M. J. Treacy for loan of the resolution test sample, to J. O. Ramey for contributions to the crystal growth effort, and to C. W. Boggs and J. T. Luck for sample preparation. This research was sponsored by the Division of Materials Sciences, US Department of Energy, under contract with Martin Marietta Energy Systems, Inc.

Received 18 August; accepted 19 October 1988.

1. Scherzer, O. *J. appl. Phys.* **20**, 20-29 (1949).
2. Treacy, M. M. J. *J. Microsc. Spectrosc. Electron* **7**, 511-523 (1982).
3. Treacy, M. M. J., *J. Microsc.* (in the press).
4. Pennycook, S. J. & Narayan, J. *Appl. Phys. Lett.* **45**, 385-387 (1984).
5. Fleischmann, H. *Z. Naturf.* **15a**, 1090-1096 (1960).
6. Pennycook, S. J., Berger, S. D. & Culbertson, R. J. *J. Microsc.* **144**, 229-249 (1986).
7. Domenges, B., Hervieu, M., Michel, C. & Raveau, B. *Europhys. Lett.* **4**, 211-214 (1987).
8. Zandbergen, H. W., Gronsky, R. & Thomas, G. *Phys. Status Solidi* (a) **105**, 207-218 (1988).
9. Ourmazd, A. *et al. Nature* **327**, 308-310 (1987).
10. Ourmazd, A., Spence, J. C. J., Zuo, J. M. & Li, C. H. *J. Electr. Microsc. Tech.* **8**, 251-262 (1988).
11. Marshall, A. F. *et al. Phys. Rev.* B **37**, 9353-9358 (1988).

Entropy catastrophe and superheating of crystals

S. Lele*, P. Ramachandra Rao† & K. S. Dubey‡

* Department of Metallurgical Engineering,
† School of Materials Science and Technology, and
‡ Department of Applied Physics, Institute of Technology,
Banaras Hindu University, Varanasi-221 005, India

Kauzmann[1] has pointed out that at a temperature (T_k) far below the melting temperature (T_m) of a crystal, the entropies of an undercooled liquid and its corresponding equilibrium crystal tend to become equal. At temperatures below T_k, the crystal would have a greater entropy than its liquid. Such a catastrophe is avoided through a glass transition of the liquid above T_k. Fecht and Johnson[2] have shown that such a transition should occur for aluminium at 0.23 T_m. A similar entropy catastrophe can also arise at a temperature, T_i^S, above T_m. Above T_i^S, the crystalline solid is once again expected to have an entropy greater than that of the liquid. Cahn[3] has considered the implications of this idea with respect to the superheating of a solid. Here we present an alternative evaluation of the two temperatures of instability, T_k and T_i^S, from experimentally measurable parameters. Results for alkali metals show that the Kauzmann-type entropy catastrophe occurs at about half the absolute melting temperature, whereas we find that the entropy catastrophe as described by Fecht and Johnson[2] occurs at twice the absolute melting temperature. For most solids, vaporization will probably intervene before the entropy catastrophe temperature above the melting temperature is reached.

Fecht and Johnson[2] considered the possibility of the isentropic temperature T_i^S coinciding with the temperature at which the volume difference (ΔV) between liquid and solid phases vanishes, for the case of both pure metals and binary alloys. Both ΔV and the entropy difference (ΔS) between these phases are partial derivatives of the Gibbs free energy difference (ΔG), with respect to pressure (P) and temperature (T) respectively. For a pure metal, if ΔS and ΔV simultaneously vanish, ΔG also becomes zero. The temperature at which $\Delta S = \Delta V = 0$ is thus the point of an equilibrium second-order phase transition from a pure solid to its liquid. In such a case, T_i^S cannot be termed a temperature of instability. However, in the case of a binary alloy, where composition provides a further variable, $\Delta S = \Delta V = \Delta G = 0$ can correspond to a temperature of instability, as discussed by Fecht and Johnson[2].

Ubbelhode[4] has discussed previous attempts to evaluate the temperature and pressure at which $\Delta S = \Delta V = 0$. Plots of ΔS and ΔV on melting as a function of pressure appear to extrapolate to a critical pressure at which melting is characterized by $\Delta S = \Delta V = 0$. For potassium this critical pressure and temperature have been estimated as 22,390 kg cm^{-2} and 498K (ref. 4). Although pressures up to 30,000 kg cm^{-2} have been attained experimentally, no phase transition or anomalies have been detected in the pressure/melting-point curves. Better methods for extrapolating ΔS and ΔV are therefore needed for predicting T_i^S and the temperature at which $\Delta V = 0$. In any case, ΔS and ΔV cannot be simultaneously zero during melting at atmospheric pressure because the corresponding isentropic and isenthalpic temperatures do not, in general, coincide. At atmospheric pressure T_i^S can still be a temperature of instability.

We have recently proposed[5] an expression for the free energy of a liquid with respect to a solid in its stable or metastable states. By a Taylor-series expansion of ΔG about its value at T_m, for constant pressure, we obtain

$$\Delta G = \Delta S^m \Delta T - \Delta C_p^m \{T \ln(T/T_m) + \Delta T\} + T_m \left[\frac{\partial \Delta C_p}{\partial T}\right]_{T_m} \{T \ln(T/T_m) + \Delta T - \tfrac{1}{2}\Delta T^2/T_m\} - \frac{T_m^2}{2}\left[\frac{\partial^2 \Delta C_p}{\partial T^2}\right]_{T_m}\left\{T \ln\left(\frac{T}{T_m}\right) + \Delta T - \frac{1}{2}\frac{\Delta T^2}{T_m} - \frac{1}{6}\frac{\Delta T^3}{T_m^2}\right\} + \ldots \quad (1)$$

where $\Delta T = T_m - T$, and ΔC_p^m and ΔS^m are the heat capacity and entropy differences respectively between the equilibrium melt and the crystal at the melting temperature. Equation (1) has been tested in cases where heat-capacity data of undercooled phases are available. For example, it has been demonstrated that ΔG of undercooled liquid gallium, magnesium and oxides of boron, silicon and germanium and their equilibrium solid phases can be determined accurately using equation (1) (refs 6 and 7). We have also demonstrated that equation (1) can predict the free energy difference between superheated body-centred cubic and equilibrium face-centred cubic modifications of iron[6].

Differentiation of equation (1) with respect to T yields an expression for ΔS of the form:

$$\Delta S = \Delta S^m + a \ln T_R - b\Delta T_R + C\Delta T_R^2 - d\Delta T_R^3 \quad (2)$$

where a, b, c and d stand for the constant coefficients involving ΔC_p and its derivatives at T_m, and are given by

$$a = \Delta C_p^m - T_m\left[\frac{\partial \Delta C_p}{\partial T}\right]_{T_m} + \frac{T_m^2}{2}\left[\frac{\partial^2 \Delta C_p}{\partial T^2}\right]_{T_m} - \frac{T_m^3}{6}\left[\frac{\partial^3 \Delta C_p}{\partial T^3}\right]_{T_m}$$

$$b = T_m\left[\frac{\partial \Delta C_p}{\partial T}\right]_{T_m} - \frac{T_m^2}{2}\left[\frac{\partial^2 \Delta C_p}{\partial T^2}\right]_{T_m} + \frac{T_m^3}{6}\left[\frac{\partial^3 \Delta C_p}{\partial T^3}\right]_{T_m}$$

$$c = \frac{T_m^2}{4}\left[\frac{\partial^2 \Delta C_p}{\partial T^2}\right]_{T_m} - \frac{T_m^3}{12}\left[\frac{\partial^3 \Delta C_p}{\partial T^3}\right]_{T_m}$$

$$d = \frac{T_m^3}{18}\left[\frac{\partial^3 \Delta C_p}{\partial T^3}\right]_{T_m}$$

where $T_R = T/T_m$ and $\Delta T_R = (1 - T_R)$. In equation (2) we have dropped terms involving ΔT_R^4 and higher-order terms. Note that both equations (1) and (2) require only the readily available values of ΔS and ΔC_p at the equilibrium transition temperature and their derivatives at T_m. These derivatives can be obtained